



HAL
open science

Light-Heat Conversion: Tracking Photothermal Energy Flow in Highly Diversified Water-Dispersed Hydrophobic Nanocrystal Assemblies

Andrea Mazzanti, Zhijie Yang, Mychel G Silva, Nailiang Yang, Giancarlo Rizza, Pierre-Eugène Coulon, Cristian Manzoni, Ana Maria de Paula, Giulio Cerullo, Giuseppe Della Valle, et al.

► **To cite this version:**

Andrea Mazzanti, Zhijie Yang, Mychel G Silva, Nailiang Yang, Giancarlo Rizza, et al.. Light-Heat Conversion: Tracking Photothermal Energy Flow in Highly Diversified Water-Dispersed Hydrophobic Nanocrystal Assemblies. *Proceedings of the National Academy of Sciences of the United States of America*, 2019, 116 (17), pp.8161-8166. 10.1073/pnas.1817850116 . hal-03003299

HAL Id: hal-03003299

<https://hal.sorbonne-universite.fr/hal-03003299>

Submitted on 13 Nov 2020

HAL is a multi-disciplinary open access archive for the deposit and dissemination of scientific research documents, whether they are published or not. The documents may come from teaching and research institutions in France or abroad, or from public or private research centers.

L'archive ouverte pluridisciplinaire **HAL**, est destinée au dépôt et à la diffusion de documents scientifiques de niveau recherche, publiés ou non, émanant des établissements d'enseignement et de recherche français ou étrangers, des laboratoires publics ou privés.

Light-Heat Conversion: Tracking Photothermal Energy Flow in Highly Diversified Water- Dispersed Hydrophobic Nanocrystal Assemblies

A. Mazzanti, Z. Yang, M. G. Silva, N. Yang, G. Rizza, P.E. Coulon, C. Manzoni, A. M. de Paula, G. Cerullo, G. Della Valle, and M.P. Pileni
Dipartimento di Fisica, Politecnico di Milano, P.zza L. da Vinci 32, 20133 Milano, Italy; Université Paris Diderot, Sorbonne Paris Cité, ITODYS, UMR 7086 CNRS, 15 Rue J-A de Baïf, 75205 Paris, Cedex 13, France; Departamento de Física, Universidade Federal de Minas Gerais, 31270-901 Belo Horizonte, MG, Brazil; Sorbonne University, Department of Chemistry 4 Place Jussieu, 75005 Paris, France; Laboratoire des Solides Irradiés, Ecole polytechnique, CEA/DRF/IRAMIS, CNRS, Université Paris-Saclay, Route de Saclay, 91128 Palaiseau Cedex, France; Istituto di Fotonica e Nanotecnologie, Consiglio Nazionale delle Ricerche, P.zza L. da Vinci 32, 20133 Milano, Italy

Significant Statement

Metal and semiconductor nanoparticles have been widely exploited in research because of their striking capacity to concentrate light energy at the nanoscale and convert it to ultrahigh speed. However, most nanoparticles are made of homogeneous materials which limits the possibility to engineer their photothermal properties. Additional degrees of freedom are provided by nano-assemblies periodically arranged nanocrystals of few nm size embedded into an organic matrix. Here we display a specific mechanism presiding over the light-heat ultrafast conversion in a highly diversified family of nano-assemblies which is intimately related to their hybrid composition at nanomedicine (photothermal therapy) and energy harvesting.

We investigate, with a combination of ultrafast optical spectroscopy and semi-classical modeling, the photothermal properties of various water-soluble nanocrystal assemblies. Broad-band pump-probe experiments with ~100-fs time resolution in the visible and near- infrared reveal a complex scenario for their transient optical response that is dictated by their hybrid composition at the nanoscale, comprising metallic (Au) or semiconducting (Fe_3O_4) nanostructures and a matrix of organic ligands. We track the whole chain of energy flow, that starts from light absorption by the individual nanocrystals and subsequent excitation of out of equilibrium carriers followed by the electron-phonon equilibration, occurring in a few picoseconds and then by the heat release to the matrix on the 100-ps timescale. Two-dimensional finite element method electromagnetic simulations of the composite nanostructure and multi-temperature modeling of the energy flow dynamics enable us to identify the key mechanism presiding over the light-heat conversion in this novel kind of nanomaterials. We demonstrate that hybrid (organic-inorganic) nanocrystal assemblies can operate as efficient nanoheaters by exploiting the high absorption from the individual nanocrystals, enabled by the *dilution* of the inorganic phase, that is followed by a relatively fast heating of the embedding organic matrix, occurring on the 100-ps timescale.

supracrystals | photothermal properties | hot carriers | nanocrystal assemblies | pump-probe spectroscopy

The last decade has witnessed an explosive growth of interest in the photothermal properties of nanostructures, for both fundamental and applied aspects (e.g., ref. 1 and references therein). A striking application is photothermal therapy for cancer, in which light, following irradiation of nanocrystals (NCs), is converted to cytotoxic heat to selectively kill cancer cells and minimize the invasive injury to normal tissues (2–7). Another notable example of the high impact of nanoparticles' photothermal properties is represented by the demonstration of novel solar photodevices for water vapor generation (8, 9) and direct sunlight-driven desalination (10).

Most of the studies in the field deal with Au nanoparticles. The development of novel and possibly more effective photothermal agents requires the understanding of the energy flow upon optical excitation of the nanostructure. For plasmonic NCs, this is well known to be governed by a cascade of dynamic relaxation processes, namely electron–electron scattering, electron–phonon scattering (and subsequent dephasing of acoustic vibrations), and phonon–phonon scattering, the latter culminating in the heat transfer from each nanoparticle to its microenvironment (11). However, unexpected and novel reactions of the medium upon light irradiation and subsequent electron relaxation have been observed in more complex systems (12–14): The combination of multiple scattering processes induces formation of either steam or a liquid vapor phase within a reduced volume even when the temperature of the bulk fluid volume remains far below its boiling point. Furthermore, hot-electron–induced photodissociation of H_2 was demonstrated by Au nanoparticles supported on SiO_2 . These recent data clearly indicate that the heat release mechanisms in composite nanomaterials are far from being fully understood and several open questions remain. This is particularly true for NC assemblies, as the interaction between NCs and the heat transfer through molecular linkers can, in principle, strongly change the thermal properties of these nanostructures and, subsequently, the dynamics of the photothermal energy conversion (1).

NC assemblies have attracted increasing interest in the past few years (see, e.g., ref. 15 for an overview). Advances in colloidal synthesis have enabled the manufacturing of NCs with uniform size, shape, chemical composition, and crystallinity, which in turn allowed their self-assembly in 3D ordered structures. Such assemblies, with a well-defined lattice configuration [e.g., face-centered cubic (fcc), body-centered cubic (bcc), etc.], are similar to atoms in crystals and are thus referred to as supracrystals (16). Depending on the experimental conditions, amorphous 3D aggregates can also be produced (17). The growth mechanism of these assemblies involves several factors (18) leading

to a complex and hard to predict behavior in the formation of shaped supracrystals that depends on the affinity between the solvent and the coating agents (19, 20). Being difficult to stabilize in aqueous solution, supracrystals are typically available and widely investigated in dried configurations, i.e., supported on a substrate. This poses a severe limitation on the development of real-world photothermal agents based on supracrystals, to be operated *in vivo*.

Very recently, some of the authors created hybrid structures, freely diffusing in water. They consist of hydrophobic inorganic NCs that self-assemble in either disordered or ordered structures due to the presence of hydrophilic organic materials (vesicles, surfactants, colloids). The synthesis of these structures exploits two basic concepts: (i) NCs standing at the interface between two immiscible liquids are highly mobile and can rapidly reach equilibrium through assembling. This enabled the demonstration of ferrite colloidosomes, i.e., shells of ferrite NCs, spherical fcc supracrystals, and egg structures, i.e., a supracrystal trapped in a colloidosome (21). (ii) The packing is governed by interdigitation processes in the organic chains of the matrix ligands. This led to the first demonstration of thermodynamically stable supra self-assemblies, i.e., supraaggregates (22–24), and water-dispersed clustered structures of hydrophobic NCs and organic molecules (25, 26). To the best of our knowledge, the energy flow upon optical excitation in water-soluble assemblies of hydrophobic NCs is largely unexplored. Here we study the specific heat release properties of 100-nm-size Au clustered structures, ferrite (Fe_3O_4) supraparticles (spherical fcc supracrystals), and Au/ferrite eggs, i.e., $(\text{Fe}_3\text{O}_4)\text{Au}_{13}$ assemblies trapped in ferrite colloidosomes. Our results indicate that the light–heat conversion in these kinds of nanomaterials is governed by a specific mechanism that relies on the intrinsic hybrid composition of the assembly involving optically active inorganic NCs and a matrix of organic ligands with relatively high heat capacity, embedded in a water environment. electron microscopy (TEM) image of individual assemblies shown in Fig. 1 *B–D* indicates a local ordering of the NCs. This is confirmed by the TEM image obtained after deposition of a drop of the colloidal solution (Fig. 1*E*), which shows that the Au NCs are well ordered in a compact hexagonal network.

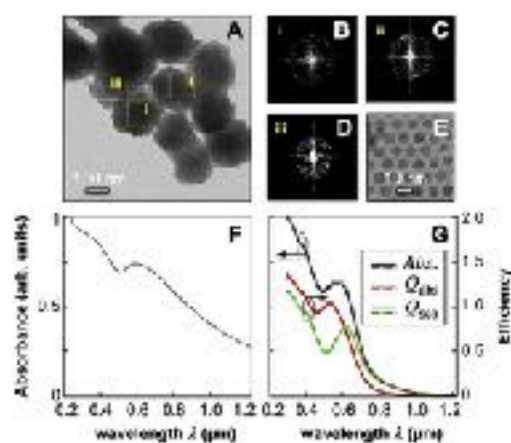


Fig. 1. (A) TEM image of Au NC assemblies produced with 10 h nucleation time and 8 min growth process time. (B–D) Samples of the FFT pattern of individual assemblies, corresponding to the areas highlighted in A. (E) TEM image of a drop of the colloidal solution of Au NCs. (F and G) Measured (F) and simulated (G) absorbance of the sample. G also shows the calculated absorption and scattering efficiencies from (solid lines) the square lattice model in Fig. 4A and (dashed-dotted lines) a triangular lattice model with the same density of NCs.

Results and Discussion

Spherical assemblies of Au NCs with ≈ 5.5 -nm diameter embedded in a matrix of 1-octadecane-thiol ($\text{C}_{18}\text{H}_{37}\text{SH}$) were synthesized (*Materials and Methods*). The average diameter of the assemblies was measured to be 160 ± 50 nm (Fig. 1A). The fast Fourier transform (FFT) pattern of the transmission electron microscopy (TEM) image of individual assemblies shown in Fig. 1 *B–D* indicates a local ordering of the NCs. This is confirmed by the TEM image obtained after deposition of a drop of the colloidal solution (Fig. 1*E*), which shows that the Au NCs are well ordered in a compact hexagonal network.

The linear optical response of Au clustered structures dispersed in aqueous solution was characterized by extinction measurements with a standard spectrophotometer. The measured absorbance (Fig. 1*F*) exhibits a pronounced peak around 600 nm, which, according to a previous study (26), is ascribable to a photonic (i.e., collective) mode of the assembly, since its spectral position scales linearly with supracrystal size.

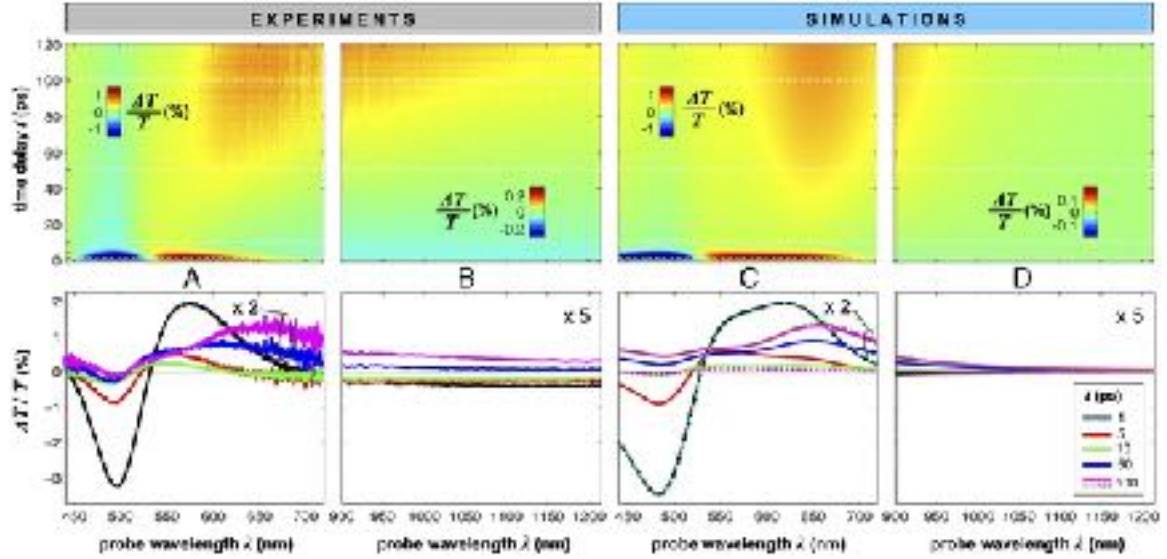


Fig. 2. Measured (A and B) and simulated (C and D) differential transmission maps T/T (Top) and map cross-sections at selected time delays (Bottom) for the water-dispersed Au clustered structures. The dotted curve in C and D is the result of a simulation which does not take into account the thermo-optical effect in the organic matrix. The dashed-dotted curves in C and D are calculated from a triangular lattice model with the same density of NCs as in the square lattice in Fig. 4A.

To investigate the energy flow upon light irradiation, we performed pump-probe experiments with ultrashort laser pulses. A 100-fs pump pulse at 400-nm wavelength, generated by frequency doubling the output of an amplified Ti:sapphire laser system (27), is used to excite the sample. A broad-band laser pulse focused on the sample at a given time delay t with respect to the pump pulse is used to dynamically probe the transient optical response. The differential transmission (T/T) spectra are recorded as a function of t and the probe wavelength λ . The results are shown in Fig. 2 A and B for visible and near-infrared probing, respectively. On the initial timescale of 10 ps, the transient signal resembles the typical T/T map recorded for plasmonic nanoparticles [spheres (28) or rods (29, 30), for example]. In particular, the map cross-sections at early time delays (black and red traces in Fig. 2 A, Bottom) show the characteristic transient spectra of isolated NCs which are dominated by shift and broadening of the plasmonic resonances (30). Moreover, these spectra exhibit a decay constant of a few picoseconds (Fig. 2A) that is the timescale of electron-phonon scattering in noble metals (31). See also Fig. 3A for the dynamics at selected probe wavelengths for delay times up to 10 ps. This demonstrates that in the ultrafast optical response the Au assemblies keep the fingerprint of their building blocks (26). However, on the longer timescales, the T/T of Au clustered structures exhibits very distinct features which, to the best of our knowledge, have not been reported in any metallic nanostructure: Instead of a monotonic decrease over time, we observe the buildup of a positive signal which is red shifted by about 100 nm (blue and magenta traces in Fig. 2 A and B, Bottom) compared with the early spectra. The temporal dynamics at selected probe wavelengths, reported in Fig. 3B, detail the onset of this broadband transient signal within about 100–150 ps. To ascertain that the observed buildup is a phenomenon that cannot be ascribed to mechanical oscillations [which, in Au NCs, are well known to have a strong impact on the ultrafast optical response on this timescale (11)], we performed pump-probe measurements on the nanosecond timescale. The results, reported in Fig. 3C, confirm that after the buildup the signal remains constant on the nanosecond timescale. However, we see a clear-cut fingerprint of mechanical oscillations with an oscillation period $T_{osc} \approx 300$ ps. We assign that oscillation to a breathing mode of the whole assembly by assuming an average speed of sound v_s of the order of 1 km/s (i.e., $T_{osc} \approx 2D/v_s$, with $D = 160$ nm), which makes sense considering the hybrid metal-organic composition (v_s in bulk gold being about 3.2 km/s). Finally, note that this transient signal was not observed in dry Co assemblies deposited on highly oriented pyrolytic graphite (HOPG) substrate (32).

To understand the origin of the observed optical features and, in particular, of the unexpected transient optical response on the 100-ps timescale, we developed a model to simulate the optical experiments. A 2D model of the supracrystal, based on the morphology detailed in Fig. 1A, is reported in Fig. 4A. Finite-element method (FEM) electromagnetic simulations retrieve the same wavelength position as in the experiment for the extinction peak in the simulated absorbance (black curve in Fig. 1G). Note that, different from the effective index approximation of ref. 26, the present model fully mimics (even though in 2D) the nanostructuring of the assembly: A square lattice arrangement of Au NCs is embedded in the $C_{18}H_{37}SH$ matrix and surrounded by a thin (3-nm) layer of dipalmitoylphosphatidylcholine

(DPPC) (Fig. 4A). For comparison, we also performed numerical simulations of a triangular arrangement of NCs with the same density (SI Appendix). The static optical response turned out to be similar to that retrieved from the square lattice configuration (compare solid curves with dashed-dotted curves in Fig. 1G). This result indicates that our assemblies behave as metaparticles, rather than finite arrays of NCs, as the collective effects are not dominated by Bragg scattering mechanisms, but rather by the onset of an effective medium, in agreement with the approximations made in ref. 26. Interestingly, despite the thickness of the assembly, the power absorbed per unit volume \rightarrow at the 400-nm excitation wavelength (Fig. 4B) is more uniform compared with that in a Au nanosphere of the same diameter. This is due to the higher penetration depth of light in the supracrystal structure (about 60 nm, which is almost four times larger than in bulk Au at the same wavelength) in view of the dilution of the metallic phase. If and how the organic phase in the assembly contributes to the energy flow dynamics and thus to the performance of the supracrystal as a nanoheater is the main subject of the study detailed below.

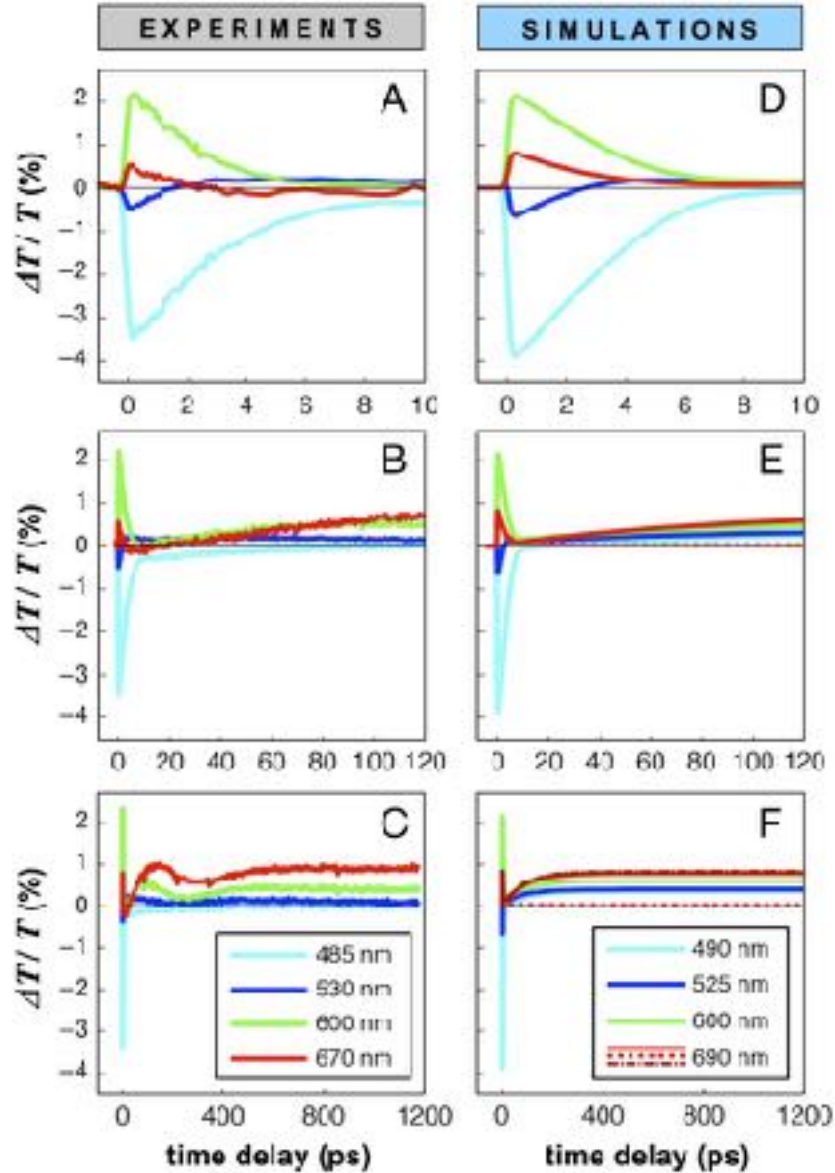


Fig. 3. Measured (A–C) and simulated (D–F) dynamics of the T/T signal at selected probe wavelengths, on the three different timescales of energy flow in the Au clustered structures. The dotted curve in E and F is retrieved without taking into account the thermo-optical effect in the organic matrix, whereas the dashed-dotted curve in F is calculated from a triangular lattice model with the same density of NCs as in the square lattice in Fig. 4A.

The model of the ultrafast spectroscopy experiments is sketched in Fig. 4C. The pump pulse is absorbed by the metallic phase of the supracrystal with a power density (per unit volume) $p_a(t)$ (SI Appendix). The pump absorption initiates a chain of energy transfer processes. In the spirit of the semiclassical models reported for plasmonic nanomaterials [noble metals (33) and heavily doped (34) and even all-

dielectric (35) semiconductors] a set of dynamical variables (usually temperatures) describing the different energy degrees of freedom is introduced and coupled together in a system of rate equations. For the hybrid metal–organic structure of Au assemblies we adopted the following four-temperature model (4TM):

$$\dot{N} = p_a(t) - aN, \quad [1]$$

$$gq_E q'_E = aN - g(q_E - q_L) \quad [2]$$

$$c_L q'_L = g(q_E - q_L) - g_0(q_L - q_0) \quad [3]$$

$$f c_0 q'_0 = g_0(q_L - q_0) \quad [4]$$

In Eqs. 1–4, the dot indicates the first derivative with respect to time, and N , q_E , q_L , and q_0 respectively are the energy density of the out-of-equilibrium electrons in the metal, the temperature of thermalized electrons in the metal, the temperature of the metal lattice, and the temperature of the organic subsystem ($C_{18}H_{37}SH$) embedding the NCs.

Note that Eqs. 1–3 basically represent the three-temperature model (3TM) which successfully describes the relaxation dynamics of Au NCs,

being $c_L = 68 \text{ J}\cdot\text{m}^{-3}\cdot\text{K}^{-1}$ the electrons' heat capacity constant, $c_L = 2.5 \times 10^6 \text{ J}\cdot\text{m}^{-3}\cdot\text{K}^{-1}$ the lattice heat capacity of gold, $g = 2.2 \times 10^{16} \text{ W}\cdot\text{m}^{-3}\cdot\text{K}^{-1}$

the electron–phonon coupling constant, and $a = 15 \text{ THz}$ the hot electrons' heating rate at 400-nm pumping (33). The 3TM of gold is then

coupled to a fourth equation, Eq. 4, that models the energy dynamics of the organic matrix of lattice heat capacity $c_0 = 1.917 \times 10^6 \text{ J}\cdot\text{m}^{-3}\cdot\text{K}^{-1}$

(36), with g_0 the coupling rate between gold phonons and the phonons of the organic matrix (to be fitted on the experimental data). In Eq. 4,

$f = V_0 / V_{Au} \pm 2$ is the ratio between the volume of the organic matrix V_0 and the volume of the metallic phase $V_{Au} = nV_i$, with n being the

estimated number of NCs in the assembly (*SI Appendix*), with $V_i = (4/3)\pi r^3$, i.e., the average volume of each NC. With the numerical solution

of Eqs. 1–4 at hand (Fig. 4 D and E), the permittivity change of the metallic and of the organic phases of the assembly is then computed as a function of the probe wavelength and time delay. In brief, $N(t)$ and $q_E(t)$ are responsible for a modulation of the interband transitions in gold, which is dominated by the Fermi-smearing mechanism due to the hot electrons at temperature $T_E(t) \gg 300 \text{ K}$; $q_L(t)$ accounts for a variation of the Drude permittivity belonging to gold free electrons, whose scattering rate with phonons linearly increases with the lattice temperature; and finally, $q_0(t)$ translates into a variation of the refractive index n_0 of the $C_{18}H_{37}SH$ matrix due to the thermo-optical effect.

The corresponding De_N , De_E , and De_L are retrieved by following the same approach detailed in previous papers on the 3TM of gold (e.g., ref. 33 and references therein). Regarding the permittivity variation induced in the organic matrix, this is computed as $De_0 = 2n_0 h D q_0$, with

$h = dn_0/dq_0$ being a negative thermo-optics coefficient, of the order of 10^{-4} K^{-1} (37) (to be fitted on the experimental data), and $D q_0$ being the

increase of the matrix temperature. Starting from the total permittivity change in the metal, $D_{Au} = De_E + De_N + De_L$, and in the organic matrix, De_0 , induced by the pump pulse, the variation of the sample transmittance is retrieved perturbatively by FEM numerical analysis (*SI Appendix*).

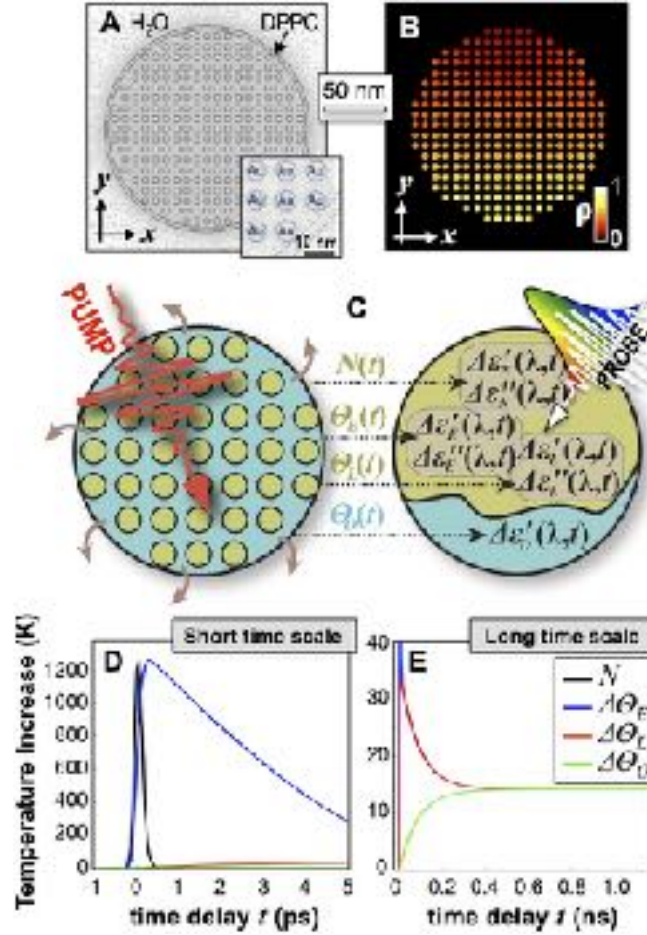


Fig. 4. (A) Model geometry and mesh structure used in the 2D numerical simulations. *Inset* shows a zoom-in of the mesh to highlight the individual Au domains. (B) Simulated power density (normalized to the peak value in the map) after the absorption of a pump pulse at 400 nm wavelength. (C) Cartoon of the two-phase assembly, made of metallic NCs (green) and organic matrix (cyan), and rationale of the 4TM used to simulate the pump-probe experiment, with each of the four dynamical variables giving rise to a separate contribution to the permittivity of the two phases. (D and E) Numerical solution of the 4TM (N normalized to the peak of $\rightarrow^i E$ for better reading) on (D) the short timescale and (E) the long timescale.

The simulated DT/T maps with best-fit parameters, $g_0 = 0.8g = 1.76 \times 10^{16} \text{ W} \cdot \text{m}^{-3} \cdot \text{K}^{-1}$, $\hbar = 7 \times 10^4 \text{ K}$, are reported in Fig. 2 C and D. Note the good agreement with the experimental maps in Fig. 2 A and B. In particular, the model is capable of reproducing both the derivative behavior of the early spectra (on the first few picoseconds timescale) and the onset of the long-lived broadband positive signal on the 100-ps timescale. It should be noted that in the numerical simulations we assumed a much lower pump fluence, $F \neq 0.3 \text{ mJ/cm}^2$, compared with the experimental value of 2.75 mJ/cm^2 . We believe that this discrepancy is mostly due to the simplification introduced with our 2D model of the supracrystal, which cannot achieve a quantitative match with the measurements, in terms of absorption and extinction cross-sections. However, the spectral (Fig. 2 C and D, *Bottom*) and temporal (Fig. 3 D–F) cross-sections of the simulated maps further confirm the capability of the model to reproduce the dynamics of the transient optical response on the various time scales and on the very broad range of wavelengths explored in our experiments. In particular, the key role of the organic matrix is ascertained and its thermo-optical response turned out to be crucial to provide a consistent interpretation of the nonlinear response of the Au clustered structures. Neglect of this contribution results in a poor agreement with the experiments, both for the spectra (dotted magenta curve in Fig. 2 C and D) and for the dynamics (dotted curves in Fig. 3 E and F), as the model is unable to reproduce the rise of the signal observed on the 100-ps timescale. Note that its prominent contribution to the DT/T is a clear-cut indication of the high temperature increase, of about 15 K according to our simulations (Fig. 4E), attained after the absorption of a single pump pulse at a moderate fluence (2.75 mJ/cm^2). This is made possible by the specific collective regime of photo-temperature generation exploited in the assembly, in agreement with what is reported in a pioneering work by Govorov et al. (38), where it has been theoretically shown that for clusters the photo-temperature is expected to increase fast with

the number of NCs. On the contrary, the lattice arrangement seems to play no role, since the simulated traces of the T/T map retrieved by a triangular configuration (dashed-dotted curves in Figs. 2 C and D and 3F) are almost superposed to the corresponding traces computed from the square configuration (solid curves in Figs. 2 C and D and 3F).

According to our model, the delayed buildup of the T/T signal on the few hundred picoseconds timescale is the signature of the final step in the light–heat conversion process that ultimately results in the heating of the matrix of organic ligands. As such, this dynamical feature in the transient optical response is expected to be an intrinsic property of any hybrid assembly of hydrophobic NCs, regardless of the peculiar nature (i.e., plasmonic or not) of their building blocks. To test this hypothesis we considered two other kinds of water-dispersed assemblies, namely ferrite supraparticles and eggs of Au/ferrite (25).

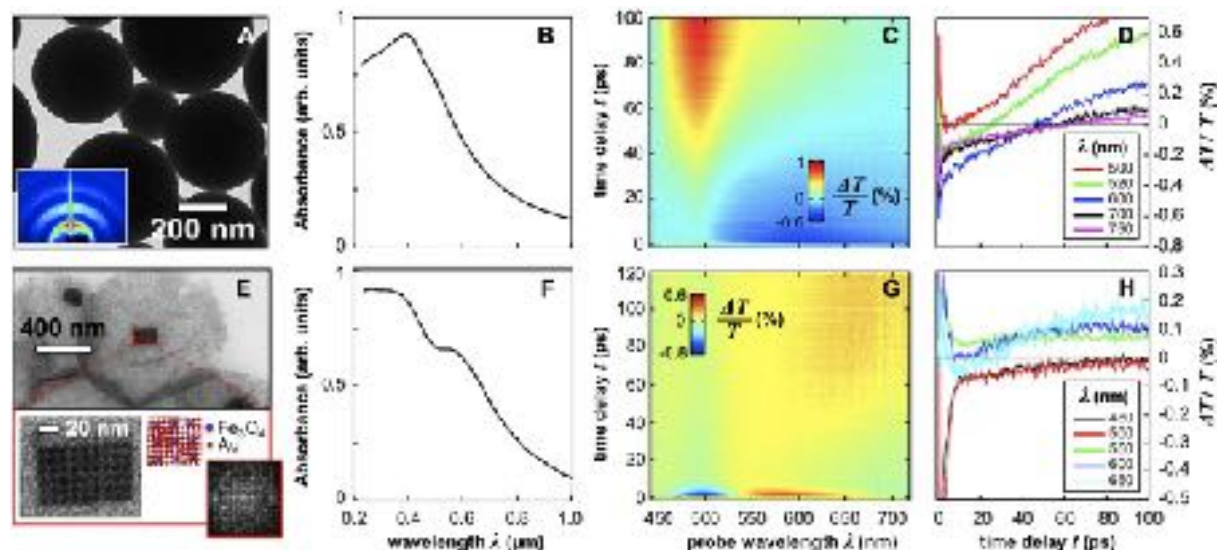


Fig.5. (A) TEM image of ferrite supraparticles. *Inset* shows the X-ray diffraction spectrum. (B) Linear extinction spectrum of the sample. (C) Measured differential transmission maps T/T . (D) Map cross-sections at selected probe wavelengths (pump fluence of about 10 mJ/cm^2 at 400-nm wavelength). (E–H) Same as A–D but for Au/ferrite eggs. E, *Inset* details the structure of the core with (*Left*) the enlargement of the TEM image in E and (*Right*) the FFT pattern and a sketch of the binary core $(\text{Fe}_3\text{O}_4)\text{Au}_{13}$ supracrystal.

As shown in Fig. 5A, spherical assemblies of ferrite NCs with an average size in the range of 200 nm are produced. The small-angle X-ray diffraction pattern (Fig. 5A, *Inset*) confirms the ordering of ferrite NCs in fcc supracrystals. These structures exhibit a pronounced extinction peak at around 400 nm (Fig. 5B) which is mostly ascribable to absorption from ferrite NCs. The differential transmission maps are reported in Fig. 5C, with map cross-sections at selected probe wavelengths shown in Fig. 5D. Note that after the exhaustion of the initial dynamics that comprise both positive and negative signals (depending on wavelength) within the first 10 ps, the longer timescale exhibits a $\Delta T/T$ that monotonically increases and reaches its maximum within a few hundred picoseconds. These are precisely the same dynamics observed in Au clustered structures (Fig. 3), the differences in the spectral profiles being related to the different kinds of resonances that dominate the linear extinction of the two kinds of assemblies.

A further evidence of the peculiarity of this mechanism is provided by Au/ferrite eggs. A TEM image of the sample (Fig. 5E) shows formation of binary core $(\text{Fe}_3\text{O}_4)\text{Au}_{13}$ supracrystals trapped into a ferrite colloidosome. The linear extinction spectrum (Fig. 5F) is characterized by a shallow peak at around 580 nm, ascribable to the plasmonic resonance of the Au NCs. Actually, the $\Delta T/T$ map (Fig. 5G) resembles the one reported for Au clustered structures, both on the short timescale and on the long one (Fig. 2A), indicating that the plasmonic resonance from the metallic phase dominates on the absorption from the semiconducting nanostructures. Also for this structure we observe that the heating of the assembly takes place on the few hundred picoseconds timescale (Fig. 5H).

Conclusions and Perspectives

In this paper we have investigated the photothermal properties of water-soluble hybrid nanoassemblies: Au clustered structures, ferrite supracrystals, and Au/ferrite eggs. An extensive experimental and theoretical investigation of the transient optical response of these

assemblies was performed with the aim of tracking the energy flow in these kinds of nanomaterials following photoexcitation. Our results indicate that Au clustered structures exhibit very peculiar features, never observed in Au NCs or even larger (polycrystalline) gold nanoparticles or Co assemblies deposited on HOPG substrate (32). In particular we show that (i) due to the dilution of the metallic phase, the penetration depth of visible light is much greater than in homogeneous metallic nanoparticles of similar size, thus enabling a high average thermal load in the whole assembly; (ii) the organic matrix, even though not directly absorbing, acts as an internal reservoir for efficient accumulation of energy within few hundred picoseconds; (iii) for moderate excitation fluences we estimated a temperature increase in the assemblies that is fully compatible with hyperthermia (7); and (iv) the above features are due to the collective regime of photo-temperature generation enabled by the assembling, since even though our model was validated on Au clustered structures, a similar behavior was experimentally observed with both Fe₃O₄ NCs self-assembled in fcc spherical supracrystals (called supraparticles) and binary supracrystals [(Fe₃O₄)Au₁₃] trapped in colloidosomes. These results provide a clear-cut indication that such hybrid nanostructures can be operated as very efficient nanoheaters, with enhanced biocompatibility due to their larger size, high stability in water, and all of the fingerprints belonging to the NCs used as building blocks.

Materials and Methods

The synthesis of clustered structures has been published recently (25, 26). In brief, Au NCs with $r = 2.75$ nm radius coated with C₁₈H₃₇SH and 5% size distribution are well dispersed in toluene. To produce shaped Au assemblies, we controlled the supracrystal growth process by subjecting the colloidal solution to a bad solvent for the alkyl chains (39). For a nucleation and growth process time of $t_1 = 10$ h and $t_2 = 8$ min, respectively, we obtained spherical assemblies with an average diameter of 160 ± 50 nm. Kranenburg et al. (24) demonstrated that the best interdigitation process is obtained with long-tail surfactant molecules and large head group surface area. Here the best interdigitation is obtained by using C₁₈ alkyl chains as a coating agent of Au NCs and DPPC characterized by two C₁₆ chains (SI Appendix). The synthesis of Fe₃O₄ supraparticles was already reported (25), and Au/ferrite eggs are obtained by revisiting the synthesis of ferrite supraparticles. Here 6.5-nm Fe₃O₄ NCs coated with oleic acid and 3.5-nm Au NCs coated with dodecanthiol are dispersed in chloroform containing octadecene, whereas the remaining procedure is unchanged. At the end of the synthesis, the colloidal solution is dispersed in water. See SI Appendix for further details.

ACKNOWLEDGMENTS. This work was supported by the advanced grant of the European Research Council (Contract 267129). M.G.S. and A.M.d.P. acknowledge financial support from the Brazilian funding agencies Conselho Nacional de Desenvolvimento Científico e Tecnológico, Fundação de Amparo à Pesquisa do Estado de Minas Gerais, and Conselho Nacional de Desenvolvimento Científico e Tecnológico. G.D.V. acknowledges the project Ministero dell'Istruzione dell'Università e della Ricerca - Progetti di Rilevante Interesse Nazionale 2015 Grant 2015WTW7J3 (Hot-electrons in self-organised plasmonic metasurfaces coupled to semiconducting MoS₂ nanosheets) for financial support.

1. Govorov AO, Richardson HH (2007) Generating heat with metal nanoparticles. *Nano Today* 2:30–38.
2. Hirsch LR, et al. (2003) Nanoshell-mediated near-infrared thermal therapy of tumors under magnetic resonance guidance. *Proc Natl Acad Sci USA* 100:13549–13554.
3. Park JH, et al. (2010) Cooperative nanomaterial system to sensitize, target, and treat tumors. *Proc Natl Acad Sci USA* 107:981–986.
4. Huschka R, Neumann O, Barhoumi A, Halas NJ (2010) Visualizing light-triggered release of molecules inside living cells. *Nano Lett* 10:4117–4122.
5. Huang P, et al. (2013) Biodegradable gold nanovesicles with an ultrastrong plasmonic coupling effect for photoacoustic imaging and photothermal therapy. *Angew Chem Int Ed* 52:13958–13964.
6. Zhihong B, Xuerong L, Yangdi L, Hongzhuo L, Kun Z (2016) Near-infrared light-responsive inorganic nanomaterials for photothermal therapy. *Asian J Pharm Sci* 11:349–364.
7. Jaque D, et al. (2014) Nanoparticles for photothermal therapies. *Nanoscale* 6:9494–9530.

8. Neumann O, et al. (2013) Compact solar autoclave based on steam generation using broadband light-harvesting nanoparticles. *Proc Natl Acad Sci USA* 110: 11677–11681.
9. Ghasemi H, et al. (2014) Solar steam generation by heat localization. *Nat Commun* 5:4449.
10. Dongare PD, et al. (2017) Nanophotonics-enabled solar membrane distillation for off-grid water purification. *Proc Natl Acad Sci USA* 114:6936–6941.
11. Hartland GV (2011) Optical studies of dynamics in noble metal nanostructures. *Chem Rev* 111:3858–3887.
12. Hogan NJ, et al. (2014) Nanoparticles heat through light localization. *Nano Lett.* 14:4640–4645.
13. Neumann O, et al. (2015) Nanoparticle-mediated, light-induced phase separations. *Nano Lett* 15:7880–7885.
14. Mukherjee S, et al. (2014) Hot-electron-induced dissociation of H₂ on gold nanoparticles supported on SiO₂. *J Am Chem Soc* 136:64–67.
15. Boles MA, Engel M, Talapin DV (2016) Self-assembly of colloidal nanocrystals: From intricate structures to functional materials. *Chem Rev* 116:11220–11289.
16. Courty A, Richardi J, Albouy PA, Pileni M (2011) How to control the crystalline structure of supracrystals of 5-nm Ag nanocrystals. *Chem Mat* 23:4186–4192.
17. Wan Y, Goubet N, Albouy P, Pileni M (2013) Hierarchy in Au nanocrystal ordering in supracrystals: A potential approach to detect new physical properties. *Langmuir* 29:7456–7463.
18. Thanh N, Maclean N, Mahiddine S (2014) Mechanisms of nucleation and growth of nanoparticles in solution. *Chem Rev* 114:7610–7630.
19. Talapin DV, et al. (2001) A new approach to crystallization of CdSe nanoparticles into ordered three-dimensional superlattices. *Adv Mater* 13:1868–1871.
20. Kalsin AM, et al. (2006) Electrostatic self-assembly of binary nanoparticle crystals with a diamond-like lattice. *Science* 312:420–424.
21. Yang Z, et al. (2016) Supracrystalline colloidal eggs: Epitaxial growth and freestanding three-dimensional supracrystals in nanoscaled colloidosome. *J Am Chem Soc* 138:3493–3500.
22. Lisiecki I, et al. (1999) Mesostructured fluids. 1. Cu(AOT)₂-H₂O-isooctane in oil rich regions. *J Phys Chem* 103:9168–9175.
23. Lisiecki I, et al. (1999) Mesostructured fluids. 2. Microstructure and supra-aggregation. *J Phys Chem* 103:9176–9189.
24. Kranenburg M, Veturoli M, Smit B (2003) Phase behavior and induced interdigitation in bilayers studied with dissipative particle dynamics. *J Phys Chem B* 107:11491–11501.
25. Yang N, et al. (2016) Dispersion of hydrophobic Co supracrystal in aqueous solution. *ACS Nano* 10:2277–2286.
26. Yang N, Deeb C, Pelouard JL, Felidj N, Pileni MP (2017) Water-dispersed hydrophobic Au nanocrystal assemblies with a plasmon fingerprint. *ACS Nano* 11:7797–7806.
27. Polli D, Lu'erc L, Cerullo G (2007) High-time-resolution pump-probe system with broadband detection for the study of time-domain vibrational dynamics. *Rev Sci Instrum* 78:103108.
28. Brown AM, et al. (2017) Experimental and ab initio ultrafast carrier dynamics in plasmonic nanoparticles. *Phys Rev Lett* 118:087401.
29. Wang X, Guillet Y, Selvakannan PR, Remita H, Palpant B (2015) Broadband spectral signature of the ultrafast transient optical response of gold nanorods. *J Phys Chem C* 119:7416–7427.
30. Silva MG, et al. (2018) Universal saturation behavior in the transient optical response of plasmonic structures. *Phys Rev B* 98:115407.
31. Sun CK, Valle'e F, Acio'li L, Ippen E, Fujimoto J (1994) Femtosecond-tunable measurement of electron thermalization in gold. *Phys Rev B* 50:15337–15348.
32. Lisiecki I, et al. (2013) Coherent longitudinal acoustic phonons in three-dimensional supracrystals of cobalt nanocrystals. *Nano Lett* 13:4914–4919.
33. Zavelani-Rossi M, et al. (2015) Transient optical response of a single gold nanoantenna: The role of plasmon detuning. *ACS Photon* 2:521–529.

34. Della Valle G, et al. (2013) Ultrafast optical mapping of nonlinear plasmon dynamics in Cu_{2x}Se nanoparticles. *J Phys Chem Lett* 4:3337–3344.
35. Gaspari R, et al. (2017) Quasi-static resonances in the visible spectrum from all-dielectric intermediate band semiconductor nanocrystals. *Nano Lett* 17:7691– 7695.
36. Tutubalina VP, Gabdrakhmanov FG, Konyukhova TM (1982) Study of the heat capacity of n-sulfides. Available at <https://webbook.nist.gov/cgi/cbook.cgi?ID=C2885009&Mask=2#ref-1>. Accessed July 2, 2018.
37. Diemeer MBJ (1998) Polymeric thermo-optic space switches for optical communications. *Opt Mater* 9:192–200.
38. Govorov AO, et al. (2006) Gold nanoparticle ensembles as heaters and actuators: Melting and collective plasmon resonances. *Nanoscale Res Lett* 1:84–90.
39. Goubet N, Richardi J, Albouy P, Pileni M (2011) Which forces do control the supracrystal nucleation in organic media? *Adv Funct Mater* 21:2693–2704.